Midlatitude cyclone compositing to constrain climate model behavior using satellite observations

Field P.R. [*], Gettelman A.[†], Neale R.[‡], Wood R.[§], Rasch P.J.[¶], Morrison H.[‖]

September 11, 2007

[*] prfield@ucar.edu, NCAR, Boulder, CO
[†] NCAR, Boulder, CO
[‡] NCAR, Boulder, CO
[§] Univ. Washington, WA
[¶] NCAR, Boulder, CO
[‖] NCAR, Boulder, CO

Abstract

Identical composite analysis of midlatitude cyclones has been carried out on both output from the NCAR (National Center for Atmospheric Research) CAM3 (Community Atmosphere Model version 3) and multi-sensor satellite data. By focusing on mean fields associated with a single phenomenon we critically appraise the ability of the CAM3 to reproduce realistic midlatitude cyclones. A number of perturbations to the control model were tested against observations, including a candidate new microphysics scheme for the next version of CAM. By subsampling composite cyclones based on system-wide mean strength (mean wind speed) and system-wide mean moisture we believe we are able to make meaningful like-with-like comparisons between observations and model output. We find that all variations of the CAM tested overestimate the optical thickness of high-topped clouds in regions of precipitation. Over a system as a whole, the model can both over- and underestimate total high-topped cloud amounts. However, system-wide mean rainfall rates and composite structure appears to be in agreement with satellite estimates. When cyclone strength is taken into account, changes in moisture and rainfall rates from both satellite derived observations and model output as a function of changes in sea surface temperature are in accordance with the Clausius-Clapeyron equation. We find that the proposed new microphysics package shows improvement to composite liquid water path fields and cloud amounts.

1 Introduction

Climate prediction science depends upon the accuracy of numerical models representing a variety of physical processes operating on diverse spatial and temporal scales. Methods for testing climate models typically consist of comparisons of global maps of annual or seasonal means or zonal means (e.g. Weare et al. 1993). While zonal and global mean comparisons are valuable tools for assessing global models, it is not easy to determine whether any discrepancies are due to the model general circulation being in error or misrepresentation of smaller scale phenomena. More recently, compositing as a function of 500 mb pressure tendency has become more popular (e.g. Norris and Weaver, 2001, Bony et al., 2004). Such compositing methods are powerful both as diagnostics and in simplifying the complex behavior of global models. One way to focus model-observation comparisons is to use the technique of compositing applied to individual phenomena. Klein and Jakob (1999) carried out the first comparison between composite satellite and composite model output of midlatitude cyclones using the European Center for Medium Range Weather Forecasts' model. In this study we use a cyclone-relative compositing approach to assess the ability of the CAM to accurately represent the spatial structure of midlatitude cyclones and their dependence upon their thermodynamic and dynamic environment.

Previous comparisons of satellite and data global model output have generally revealed bias in cloud representations. Norris and Weaver (2001) compared ISCCP data with the NCAR community climate model version 3. They showed that for Pacific summer time midlatitude regions the CCM3 overpredicts cloud top height and cloud optical thickness in regions of large scale ascent, while they find the opposite for regions of subsidence. They attribute the overproduction of cloud in the regions of ascent to the lack of subgrid variability in vertical velocity and hence humidity.

Similarly, Webb et al. (2001) and Lin and Zhang (2004) both compared ISCCP climatologies with various climate models and found at midlatitudes that the cloud optical thickness was overestimated for high topped clouds. Klein and Jakob (1999) found that while the model generally reproduced the various cloud types and their cyclone-relative positioning, the model exhibited differences to the observations when the optical thickness characteristics were assessed.

The CAM3 hydrological behavior was recently reviewed by Hack et al. (2006). They note that CAM3 over predicts cloud liquid water path (LWP) in the midlatitudes when compared to satellite derived products; consistent with an overprediction of optical thickness of clouds in GCMs. In contrast, the zonally averaged precipitation rates from CAM3 are more similar to the Climate Prediction Center Merged Analysis of Precipitation (CMAP) product (Xie and Arkin 1997) at midlatitudes, although the maxima are more poleward in CAM3 suggestive of a poleward bias of the storm tracks. Similarly, the column integrated water vapor from CAM3 in midlatitudes agrees to within 10% of the National Aeronautics and Space Administration Water Vapor Project (NVAP) product (Randel et al. 1996).

Another aspect of midlatitude cyclones that has received attention recently because of the potential impact to population centers in temperate regions is the location and intensity of the cyclones located in the midlatitude storm tracks. One avenue of investigation has focused on using re-analysis data to determine whether there has been any change in the storm tracks over the last few decades (e.g. Paciorek et al., 2002; Wang et al. 2006), while the second avenue has attempted to predict the changes in storm tracks that might be expected under climate change (e.g. Carnell and Senior, 1998; Sinclair and Watterson, 1999; Fyfe, 2003; Geng and Sugi, 2003; Bengtsson et

al. 2006). Inspection of re-analysis data for the last half of the 20th century led Paciorek et al. (2002) to suggest that while there has been little significant change in the numbers of cyclones, the occurrence of more intense cyclones has increased. Wang et al. (2006) similarly analyse the latter half of the 20th century and also report on winter increases in the frequency of occurrence of intense cyclones in the North Pacific midlatitude and North Atlantic at higher latitudes, while North Atlantic midlatitude display some decrease. This behavior in the North Atlantic is ascribed to the poleward migration of the storm track.

Investigation into changes expected under climate change using a variety of climate models run at different resolutions have yielded varying predictions. These have ranged from increased frequency of stronger cyclones (Carnell and Senior, 1998; Fyfe 2003; Geng and Sugi, 2003) to small changes in the numbers of instense storms (Bengsston et al. 2006) through to a reduction in the frequency of stronger storms (Sinclair and Watterson, 1999). Both Sinclair and Watterson (1999) and Bengsston et al. (2006) attribute these apparent differences to the cyclone location and tracking techniques employed. However, all of the studies suggest, in agreement with observational work (e.g. Yin et al. 2005, Fu et al. 2006), that there will be a poleward shift of the storm tracks and that total numbers of cyclones will decrease as a result of reduced baroclinicity. This variability in predictions provides motivation for assessing whether global models are producing realistic simulations of these systems at the scale of individual cyclones.

The study of composite cyclones by Field and Wood (2007a, hereafter FW07) used satellite derived observations to partition the cyclones. It was asserted that *i) On average a cyclone will exhibit similar precipitation and cloud structure to another cyclone if the thermodynamic and*

mesoscale dynamical environments are comparable. ii) The thermodynamic and mesoscale dynamical environment for each cyclone can be categorized by two metrics that represent the mean atmospheric moisture and the mean cyclone strength. They found that a simple warm conveyor belt model adequately described the change in cyclone-wide mean rainfall rate as a function of cyclone moisture and strength. However, high-topped cloud was more complicated and was better correlated with cyclone strength than with moisture.

In this study we have focused on comparing satellite observations and CAM3 representations of composited midlatitude cyclones. By compositing cyclones based on their strength and moisture we believe we are able to compare like-with-like. In this way we hope to be able to avoid any differences in climatologies (e.g. different storm tracks) between the model and the satellite observations. Section 2 briefly describes the CAM3 model and modifications that we have used. Section 3 outlines the compositing methodology. The satellite data used for comparison will be summarized in section 4, and the comparison with the model data will follow in section 5. The Discussion and Conclusions form sections 6 and 7.

2 Model description

2.1 CAM3 control

Collins et al. (2006) describes the current NCAR (National Center for Atmospheric Research) Community Atmosphere Model (CAM3) but for the purposes of this paper we will outline some aspects of the microphysics implementation and treatment of cloud fraction that will be relevant

to the discussion. The microphysical representation in CAM3 is described in detail by Rasch and Kristjanson (1998) and introduced a prognostic condensed water variable with diagnostic phase separation based on temperature such that the condensed water liquid fraction varies from 1.0 at -10C to 0.0 at -40C (-30C in the original implementation). Each phase consists of a 'cloud' species that has negligible fallspeed and a 'precipitation' species that has a fall speed appropriate for the phase. The cloud fraction approach used in the model is described by Zhang et al. (2003) and is a diagnostic scheme based on the Slingo (1987) quadratic cloud fraction relation with an associated critical grid box mean relative humidity for the existence of cloud.

The model runs presented here have been made using the CAM3 finite volume dynamical core at a grid spacing of 0.9 degrees latitude, 1.25 degrees longitude, 26 vertical levels (surface to 3 mb) and a timestep of 30 minutes. One run carried out using 4 by 5 degree grid spacing to assess the effect of resolution on cyclone representation in the CAM, was used. The radiation scheme is described by Collins et al. (2006) and the overlap scheme assumed for the subgrid deployment of the clouds is an important aspect. For the experiments described here, the maximum-random overlap assumption was used.

2.2 CAM3 modifications

We ran a number of different configurations of the CAM3 in an attempt to attribute physical or model parameterization differences to resulting differences in the model output. The configurations were: a) *ssat* this is a modification of the cloud fraction scheme that requires greater grid box relative humidity to produce the same cloud fraction as in the standard CAM3. This modification

was used in Gettelman and Kinnison (2007) and is a variation of the Slingo (1987) cloudfraction scheme. In the original scheme cloud begins to form at a grid box mean relative humidity with respect to ice of 90% and covers 100% of the grid box when the relative humidity reaches 100%.The modification has the effect, for temperatures colder than -30C, of increasing the critical relative humidity to form cloud when ice is present from 90 to 100% and complete cloud cover occurs when the relative humidity is 120% over ice. b) *4x5* a low horizontal resolution run often used for paleoclimate investigations with a horizontal grid spacing of 4 degree in latitude and 5 degrees in longitude. c) *nodeep* the Zhang and McFarlane (1995) deep convection parameterization was turned off, with convection handled only by the 'local' convective scheme (Hack 1994). d) *noconv* both the deep and 'local' subgrid convection schemes were disabled. e) *micro* the microphysical scheme of Morrison and Gettelman (2008) was used. The new stratiform microphysics scheme in CAM predicts the number concentrations and mixing ratios of cloud droplets and cloud (small) ice. The prediction of both mixing ratio and number concentration allows the effective radius to evolve freely in the model, which is critical for cloud radiative forcing. The scheme also diagnoses both the mixing ratio and number concentration of rain and snow. This allows for the differentiation of precipitation regimes; namely, shallow clouds with drizzle versus deeper cloud systems with melted snow and large rain drops (Gettelman et al. 2008). The scheme includes a number of microphysical processes that transfer water between vapor, clouds, and precipitation (e.g., condensation, autoconversion, accretion). It also includes a physically-based treatment of the partitioning between liquid and ice in subfreezing conditions based on the relevant process rates (freezing, and the Bergeron process, i.e., transfer of liquid to ice due to lower ice saturation vapor pressure). Other microphysics schemes in GCMs typically use simple temperature-based partitioning to separate liquid and ice (e.g., DelGenio et al. 1996; Rasch and Kristjansson 1998).

When running the models with prescribed SSTs, the global radiative balance of the model is not vital because the ocean acts as an infinite energy source/sink. However, the models need to be configured sufficiently well so that unrealistic global warming or cooling occurs in fully coupled ocean-atmosphere runs. Therefore it is desirable that the atmospheric component of the model is in approximate global radiative balance at the top of the atmosphere. We note that model configurations *control, ssat, 4x5, micro* were ran in approximate global radiative balance at the top of the atmosphere (± 2 W m^{-2}), while the *nodeep, noconv* configurations were not balanced radiatively (± 10 W m^{-2}).

For the *control, ssat, 4x5* configurations the model was run for ten years to establish a climatology. For the *nodeep, noconv, micro* configurations it was decided that five years would be sufficient due to computational costs. For all of the configurations we analyzed the last three model years (36 x 30 days) of the data. All the configurations were run as a standalone atmosphere with a predefined data ocean of observed SSTs. Because different years were used in the analysis of the model results and satellite data we assessed any differences introduced by the variation in observed SSTs by comparing the *control* run analysis for two different 3 year periods. We found that using different years for the analysis did not introduce any biases that might arise from different SST climatologies. The results are discussed below in more detail.

3 Model output compositing

From the final three years of the runs daily instantaneous output was obtained at 0 UTC for the following two dimensional fields: mean sea level pressure, 10 m horizontal winds, integrated water vapor column, rainfall rate, liquid water path, sea surface temperature, integrated column relative humidity (FW07), cloud top temperature and cloud types generated from the ISCCP simulator embedded in the CAM3 (Klein and Jakob, 1999) which predicts what a satellite would see given subgrid assumptions such as cloud overlap geometries (assumed to be max random overlap in this case. We note that the ISCCP simulator only uses the parameters associated with non-precipitable species to estimate the radiative effects of clouds. The satellite observations of clouds used for the comparison employ MODIS data. MODIS can detect a minimum optical depth of 0.1–0.2 (Choi et al. 2005) and so we have made use of all of the optical depth bins provided from the ISCCP simulator. For cloud types obtained with satellite data the pressure categories used were $p_{top} < 440$ hPa, $440 < p_{top} < 710$ hPa, $p_{top} > 710$ hPa for high-, mid- and low-top cloud respectively. Cloud optical depth thresholds used to classify clouds into optically thin, medium, and thick types are $\tau < 5$, $5 < \tau < 25$, and $\tau > 25$ respectively for water clouds, and $\tau < 3.75$, $3.75 < \tau < 25$, and $\tau > 25$ for ice clouds. These categories are slightly different to those used by ISCCP, but they are as close as is possible given the joint histogram bins used in the MODIS Level 3 data (Oreopoulos, 2005). For the CAM output we used the same pressure thresholds (emissivity adjusted cloud top pressure) and the same optical thickness thresholds as used for the water clouds.

The 10 m horizontal winds were computed using a two stage iterative technique to compute correction factors for the lowest model layer winds to estimate the 10 m winds based on stability and the height of the lowest model layer (CCSM3.0, coupler v6.0 documentation, available at

http://www.ccsm.ucar.edu/models/ccsm3.0/cpl6/).

For compositing the model cyclones we followed the same method used for the satellite and reanalysis data (FW07) To locate the cyclones we use a surface pressure and derive first and second order derivatives that are thresholded to obtain candidate gridpoints to represent the cyclone center ($\frac{dp_0'}{dx}\frac{dp_0'}{dy} < 4 \times 10^{-5}$ hPa^2 km^{-2} and $\frac{d^2p_0'}{dx^2} + \frac{d^2p_0'}{dy^2} > 9 \times 10^{-5}$ hPa km^{-2}). These candidates were then filtered to locate the maximum negative anomaly within a 1900 km radius with a p_0 <1015 hPa (FW07 used 2000 km, but here we reduced it slightly to include slightly more cyclones per year). Therefore a single cyclone throughout its evolution could be identified as separate systems on consecutive days. From the global analysis of cyclone locations we focus the analysis in this paper upon four subregions: North Pacific (30-55°N, 145°E-165°W); North Atlantic (30-60°N, 10-50°W); South Pacific (30-55°S, 120-180°W); South Atlantic (30-55°S, 50°W-10°E). Cyclone centers must be located within these domains to be considered for analysis.

For each cyclone the model output fields (initially all on a $0.9^\circ \times 1.25^\circ$ grid, apart from the *4x5* runs) are translated and regridded using bilinear interpolation onto a 4000 km by 4000 km domain (x, y are the eastward and northward coordinates respectively) with 100 km grid spacing and the cyclone located centrally ($x = 0, y = 0$).

After regridding data onto the cyclone-centric domain, statistics are derived from the resulting ensemble of cyclones. We examine cyclone properties as a function of cyclone strength and atmospheric moisture metrics that are defined as follows. *Cyclone strength*, $\langle V \rangle$, is determined as the mean 10 m wind speed, within a circle of radius 2000 km centered on the cyclone. Our

atmospheric *cyclone moisture* metric, $\langle WVP \rangle$, is similarly defined as the mean water vapor path within a circle of radius 2000 km centered on the cyclone. We choose a measure of the atmospheric moisture content as an additional metric because it determines the availability of moisture for the development of cloud and precipitation and it is strongly dependent on sea surface temperature (see FW07) and so will change with increasing global temperatures.

Cyclones in the southern hemisphere are similar to their northern hemisphere counterparts for similar cyclone strength and atmospheric moisture (FW07). We therefore reflect the southern hemisphere cyclones about a zonal axis ($x \rightarrow x, y \rightarrow -y$) and combine all of the cyclones in a northern hemisphere sense. Conditional sampling of the cyclones into three moisture categories ($\langle WVP \rangle$: 10-18,18-21,21-33 kg m^{-2}) and three strength categories ($\langle V \rangle$: 4.9-6.95, 6.95-8.14, 8.14-12.3 m s^{-1}) matching those used in FW07 produces nine composite categories Further conditional sampling within an $\langle WVP \rangle$,$\langle V \rangle$ ellipse (see Field and Wood, 2007) ensures that there is no monotonic variation in strength for a given strength category and different moisture categories or vice versa. The cyclone database is finally filtered to remove systems where the fraction of non-missing SSTs colder than 278 K, as determined from AMSR, exceeds 0.3. This filtering is performed so that potential problems with the rain rate estimates related to near-surface freezing levels are avoided.

Cyclone-wide composite means (within 2000 km radius of center) of a number of parameters have been generated. FW07 discussed systematic errors associated with the satellite measurements. Their conclusion was that if there are no systematic biases in the observations, then given the number of observations combined at each point in the composites the random error is small

($< 1\%$ for $\sim$100 member composite). Therefore the error bars represent the error in the mean at 95% confidence due to variability from cyclone to cyclone. These errors are obtained by calculating the weighted mean of the standard error of the means at each point in the composite, and then dividing by the square root of the degrees of freedom in the composite field (typically 5–20) that are determined using the spatial equivalent of the temporal autocorrelation method of Leith (1973).

4 Review of the satellite observations

Here we briefly revisit the satellite data described in FW07 (and a correction that was issued: Field and Wood, 2007b) that is used here for comparison. The main finding from the satellite observations is that the cyclone-wide mean rainfall rates are consistent with a simple warm conveyor belt argument:

$$R_{wcb} = c \langle WVP \rangle \langle V \rangle , \tag{1}$$

where $c = wk/A_c$ is a constant that is composed of the areal extent, A_c, of the cyclone (2000-km radius circle), the composite width, w, of the warm conveyor belt, and a constant, k. In FW07 c was found that provided the best correlation between the composite mean rainrate and the product of the composite mean moisture and strength. Figure 1 shows the composite mean rainrates from the satellite observations for the 3 strength categories within the most moist category and 3 moisture categories for the greatest strength category. The observations show that rain is generally located to the east of the cyclone center in a rough comma shape. The heaviest rain tends to occur just slightly north east of the center and then arc around to the south, reminiscent of the warm

conveyor structure suggested by Harrold (1973). It can be seen that increasing either strength or moisture produces an increase in rainfall rates. The inset figure shows the observed mean cyclone composite rainfall rates plotted against the value obtained from eq 1 when $c = 0.023$ (R_{wcb} in mm day^{-1}, $\langle WVP \rangle$ in kg m^{-2}, and $\langle V \rangle$ in m s^{-1}).

In contrast to the behavior of the rainfall patterns with cyclone strength and moisture, the high-top cloud fraction was found to be positively correlated mainly with cyclone strength, exhibiting smaller variation with changes in moisture. This result was attributed to a possible decoupling between upper and lower tropospheric moisture.

5 Model - satellite comparisons

Because we used two different groupings of years for the model analysis that are themselves different from the two years over which the satellite data were obtained, we would like to know if there is any effect introduced by the different SSTs that were present. As a test we carried out the same analysis of the *control* run data for two different periods: 1979-1981 and 1984-1986. We found that the distribution of cyclones within the 9 strength and moisture categories was similar and that cyclone mean composite values for rainfall rate, high topped cloud fraction and RHcol are typically also very similar. In some of the following figures we have plotted both *control* run results to provide an estimate of variability introduced by using results from differing time periods.

The formation of high clouds is a useful tuning process for climate models. By modifying the critical gridbox mean relative humidity ($\mathrm{RH_{crit}}$) at which clouds begin to form, the amount of

high cloud and hence the planetary albedo can be controlled. This effect can be used to fine tune a climate model to balance the incoming and outgoing radiation. In the CAM the radiation only interacts with the non-precipitating 'cloud' ice and water. The condensed water in the precipitating species may have some impact on the optical thickness of clouds, but at present is not considered. Thus, there is a difference between what the CAM sees as radiatively important and what the actual cloudy atmosphere sees as radiatively important i.e. possibly a much wider range of hydrometeor sizes including precipitation particles. Therefore, we need to bear this difference in mind when we compare the high cloud amounts and their subdivision into optical thickness categories.

Figure 2 shows the composite mean high cloud fractions for the greatest strength category and medium moisture category. The satellite data shows the 'comma-shaped' high cloud shield associated with the fronts out to the east of the cyclone center. All of the models capture this broad pattern, but the *control*, *ssat* and especially the *4x5* runs produce too much high cloud. The result for *ssat* is surprising given that greater relative humidity at temperatures colder than -30C is required to produce cloud. The *nodeep* and *noconv* runs are not radiatively balanced, but do produce less cloud. The *micro* run is radiatively balanced and produces less high cloud than the *control*, but still more than the satellite observations suggest. We have examined these differences further by subdividing the high-topped cloud category into 3 optical thickness categories (fig. 3, left). To maximize the amount of data in each cloud thickness category we took all of the cyclones from the NP region regardless of moisture or strength. The satellite observations show the largest contribution from the intermediate optical thickness, cirrostratus, category. In contrast, all of the model results show that the contribution from the thickest cloud is most significant. For the *micro*, *4x5* and *control* there is also some contribution from the thinnest, cirrus, category. Similar figures have

been generated for the mid-top and low-top cloud categories, but interpreting the results for lower cloud tops is difficult because of the compounding masking effects of the higher clouds. Even though the ISCCP simulator does take account of cloud overlap, the cascade effect of the higher clouds can be difficult to unravel. Nevertheless, the models tend to produce hardly any mid-top cloud (fig. 3, center), while the satellite suggests 10-20% cloud fractions of the intermediate optical thickness category to the west of the cyclone center. For the low-top cloud (fig. 3, right) the models tend to overpredict the intermediate and greatest optical thickness cloud, while the satellite observations suggest modest amounts of optically thin low-top cloud. These model differences may be related to problems with the convective detrainment parameterization, but more tests will be required.

Returning to the total high-top cloud fraction we have plotted the mean composite values as a function of cyclone strength (fig. 4) for the satellite and model results (the squares for the greatest strength category are obtained from the composite fields depicted in fig. 2). Fig. 4 shows that the *4x5* and *noconv* runs are outliers that generate too much and too little high-top cloud amounts, respectively. For the other model configurations the agreement with the observations is better, but the *control* appears slightly high. Bearing in the mind the sizeable error in the mean, the results for *micro*, *nodeep* and *ssat* are in satisfactory agreement with the satellite observations. All model simulations correctly predict increasing high clouds with increasing cyclone strength, but the sensitivity in each case varies considerably. Comparing the spacing between symbols for a given strength is suggestive that the model high-top cloud fractions vary more with moisture than the satellite observations.

Rainfall rates derived from microwave measurements are compared with the model results for the strongest strength category and the medium moisture category in fig. 5. All show rain located in a 'comma' shaped region to the east and southeast of the cyclone center. The models show considerable skill in predicting the extent and magnitude of the rain, with the *noconv* run generating the greatest averaged rainfall amounts. Fig 6a shows the results for all 9 strength and moisture categories (the solid squares representing the greatest strength category are obtained from the composite fields depicted in fig. 5). Within the error in the mean, all of the model results agree with the satellite observations across all the strength categories. It is interesting that the *noconv* runs produce similar rainfall rates to the other model runs suggesting that the large scale transport adjusts to compensate for the lack of subgrid transport. The only difference appears to be that the satellite derived values exhibit greater variation with moisture than the models. It was shown in section 4 that in the observations the product of the cyclone moisture and strength was directly proportional to the mean composite rainfall rate. This behavior was attributed to the action of the warm conveyor belt that lifts warm moist air around the eastern boundary of the cyclone to be precipitated as it condenses. Fig. 6b shows that the warm conveyor belt model used for the satellite data also adequately describes the model results within the range of the typical error bars. Finally, fig 6c shows the variation of mean composite WVP with SST. It can be seen that the model and satellite results are all in agreement with the exception of the *noconv* results that are offset to higher SSTs. Examination of the *noconv* results shows that the lack of subgrid vertical moisture transport leads to excessive moisture in the lowest model levels and a lack of transport of this moisture to higher levels. This means that to find cyclones with similar mean moisture values in the nonconv results to those from runs with convection requires searching over warmer SSTs.

We have considered the change of the mean composite WVP and rainfall rate in terms of what might be expected from the Clausius-Clapeyron relation. If we consider the saturated water content at the surface, q_{s0}, then the Clausius-Clapeyron relation tells us that $d\ln(q_{s0})/dT = 0.065K^{-1}$. For the column integrated WVP we also need to consider the change in moisture scale height, S, with surface temperature (SST), T.

$$WVP = S\rho_{air}q_{s0}RH_0 \tag{2}$$

where RH_0 is the relative humidity at the surface that is assumed to be insensitive to temperature and ρ_{air} is the air density. By differentiating eq. 2 with respect to temperature when $S = (R_vT^2)/(L\Gamma)$ (Weaver and Ramanathan, 2005) and $dq_{s0}/dT = (Lq_{s0})/(R_vT^2)$, where R_v is the specific gas constant for water vapor, L is the latent heat of vaporisation and Γ is the moist adiabatic lapse rate, we obtain:

$$\frac{dln(WVP)}{dT} = \frac{L}{R_vT^2} - \frac{dln\Gamma}{dT} + \frac{2}{T} \tag{3}$$

The value of the first term on the right hand side is 0.065 K^{-1}, i.e. the standard increase of 6.5% per K of saturation specific humidity associated with the Clausius-Clapeyron equation.. The second and third terms have values of 0.02 and 0.007, respectively for temperatures of $\sim$290 K. Therefore, the fractional change in WVP is $\sim$ 0.09 K^{-1} . Curves assuming changes based on both 0.065 K^{-1} and 0.09 K^{-1} have been overplotted on WVP data from the satellite and model results in fig. 7a (points for the medium strength and moisture category all collapse to the center of the plot). For each cyclone strength category the ratio of WVP for the moist and dry categories is referenced to the medium moisture category and plotted as a function of the deviation in sea surface temper-

ature (SST). The standard errors shown result from the propagation of errors. It is clear that the mean composite WVP for midlatitude cyclones follows the Clausius-Clapeyron relation. A similar analysis was carried out for the rainfall rates. Again it appears that the 0.09 K^{-1} relation agrees slightly better with the data, fig. 7b shows that the mean composite rainfall rate from midlatitude cyclones also follows the Clausius-Clapyeron relation.

It is known that the CAM3 cloud liquid water path (non-precipitating droplets) is overestimated when compared to zonal means derived from satellite observations (e.g. Hack et al. 2006). Figure 8 compares cloud liquid water paths derived from AMSR-E microwave measurements with the model results for the strongest strength category and the medium moisture category (unfortunately we are not able to compare ice water paths). As expected, the locations of the maximum liquid water path are highly correlated with the rainfall patterns shown in fig. 5. It is clear that the *control* run generates too much liquid water path, while the result from the new microphysics is much more comparable with the satellite derived values in agreement with results shown by Gettelman et al. (2008). Similar results are seen in the other strength and moisture categories. Without further tests of the *micro* model it is not possible to discern the exact cause of the improved agreement with observations. Many effects such as the transfer of liquid to ice and autoconversion from cloud species to precipitation species may have played a role. Perhaps more fundamentally is the fact that the *micro* scheme predicts smaller cloud particle sizes. This allows the CAM with the new microphysics to act radiatively similar to the *control* version but with less liquid water path (and less ice water path).

6 Discussion

It is encouraging that the mean composite rainfall rates from the models show good agreement with the observations, even for the low resolution *4x5* run. This suggest that much of the dynamical structure important for the generation and evolution of realistic midlatitude cyclones is represented in these models. Even with the total removal of subgrid moisture transport via the convective schemes (noconv) the rainfall structure and magnitude was similar to the other model results. Fundamentally this indicates that in midlatitudes baroclinic disturbances govern how much latent energy is released, and hence rain is produced. Although it is clear that the production of rain and associated clouds will feed back onto the dynamics through radiative effects, both immediately through the intensification of the storm, and also on seasonal and longer (climate) timescales, through the modification of baroclinicity, in general. Because there is good agreement between the model and observations on a cyclone-centric basis, this suggests that the differences seen in the CMAP zonally averaged precipitation comparison with CAM3 at midlatitudes arise from variations in the storm track climatology between the observations and model.

With the introduction of the new more detailed microphysics scheme, the CAM3 is now able to reproduce the same top of atmosphere radiances as the *control* CAM3 but with lowered LWP. In the deep stratiform clouds associated with the fronts, the relatively large amounts of cloud ice and snow present would tend to inhibit the activation of new droplets and quickly remove existing liquid water through riming and the Bergeron-Findeisen process.

Although the rainfall behavior of the composite cyclones is in good agreement with the observations we have not tested any differences in climatology, such as the latitudinal preference of the storm tracks. The upper left panel in figure 9 shows the distribution of mean strength and

moisture values for the cyclones in the satellite dataset and the subsample used for the analysis (gray points). Plots for the model runs produce similiar distributions, but it is easier to discern differences by looking at the relative frequency of cyclones found within each of the 9 strength and moisture categories. For the satellite observations the most populous categories lie along the diagonal from the weakest and most moist to the strongest and driest categories. For most of the model results the cyclones appear to be skewed to the higher strength categories. The exception is the *4x5* run that appears quite similar to the distribution for the satellite observations. These differences could indicate actual variations in the climatology of midlatitude cyclones, and the poleward bias of the storm tracks would be consistent with stronger storms. Or the difference may simply be the result of the method used to locate the cyclones that may reflect the characteristics of the different pressure fields used.

Allen and Ingram (2002) showed that for global mean temperature changes the change in precipitation is about half that expected from arguments based on the Clausius-Clapeyron relation. They suggest that the global precipitation is not just controlled by moisture availability, but also the ability of the atmosphere to radiate away extra heat produced by increases in precipitation; it is the inefficiency of this radiative cooling that limits the increase in global mean precipitation with increasing surface temperature. We saw here that the changes in composite mean rainfall rates with SST are consistent with the Clausius-Clapeyron relation on the scale of midlatitude cyclones. Therefore, to skew the global response of precipitation to SST change away from that expected from the Clausius-Clapeyron relation implies that either the precipitation in the tropics increases much more slowly than the Clausius-Clapeyron relation to compensate for any Clausius-Clapeyron behavior in midlatitudes and/or that the climatology of midlatitude cyclones would have to adapt

to result in the much more modest variation of global precipitation with SST seen in GCMs.

Fig. 3 showed convincingly that the model tends to produce more thick high-topped cloud than the observations. Recall that the CAM radiation (and hence ISCCP simulator) only sees the non-precipitating cloud species, whereas the satellite sees contributions by particles from a much broader range of sizes. Because these high topped clouds can be used to tune the radiative balance of a climate model, the lack of contribution from precipitation sized particles may result in over compensation by the smaller cloud particles, leading to more extensive high-topped cloud than is observed. Because *micro* leads to lowered liquid water path, this effect could potentially be exacerbated as the contribution from the precipitation sized particles becomes relatively more important. It will be interesting to check this assertion, but that falls outside of the scope of this present study. The total mean composite high topped cloud fractions were not inconsistent with the observations (fig. 4), but the consistently 50% higher values seen in the *4x5* results may be a concern for paleoclimate studies that use lower resolutions (Yeager et al. 2006). The reason for this big difference is most likely due to the the critical relative humidity used in the macrophysical parameterization being set to the same value as the higher resolution models (RH_{crit}=0.90). The new stratiform microphysics shows some decrease in high topped cloud, and this is again likely related to the RH_{crit} value used (RH_{crit}=0.93). The new stratiform microphysics made it possible for the RH_{crit} to be increased without adversely affecting the radiative balance of the model primarily due to the smaller effective radii that this scheme passes to the radiation parameterization.

Lin and Zhang (2004) also found that in the storm tracks the CAM2 model (similar clouds to CAM3) overpredicted high-topped optically thick and thin cloud, overestimated low-topped

optically thick cloud, but underestimated mid-topped and low-topped, optically medium and thin cloud. They suggested that radiatively, the CAM2 produces the right radiation at the top of the atmosphere, but for the wrong reasons. Similarly, Webb et al (2001) also find that some global circulation models tend to overestimate high-topped optically thin and thick cloud. They suggest that the overlap assumptions used by the radiation may play an important role: a random overlap assumption may lead to a higher occurrence of intermediate optical thickness high-top clouds than a maximum-random overlap scheme such as that used in the CAM3. The second possibility raised by Webb et al. (2001) is that mass flux convective schemes could lead to increased cloud amounts at high altitudes. It is clear that the convective parameterizations also play a role in transporting water to higher levels within the troposphere to potentially form cloud as indicated by the much lower cloud fractions produced by the *noconv* results.

The analysis method presented here provides a storm focused approach to comparing model output with observations. The advent of extensive satellite borne multi-sensor global data mean that such an approach could be potentially used to investigate diverse phenomena ranging from hurricanes to the Madden-Julian Oscillation.

7 Conclusion

Model and satellite data were composited in the same manner as a function of cyclone strength and cyclone moisture to facilitate a comparison of modelled and observed midlatitude cyclones. The comparison indicated that the rainfall rates produced by the CAM3 (all variations) were consistent with those derived from satellite microwave observations. This agreement implies that any

difference in zonal or global averages of precipitation are most likely due to differences in the climatology of midlatitude cyclones rather than the representation of individual events. It is unknown if the differences observed in the cloud structure could lead to changes sufficient to be the source of this difference.

The new microphysics implementation produced a better agreement between the model results and the composite liquid water path obtained from the satellite observations.

High-top cloud fractions for all the CAM3 variations (apart from *noconv* and 4x5) produced similar amounts to the satellite derived values. However, the comparison of clouds from satellite and model output revealed that the model high-top clouds appreared optically thicker than the observations suggest. The mid- and low-topped clouds from the model also displayed a propensity to higher optical thicknesses than the observations suggested.

For individual cyclones, when cyclone strength was taken into account, variations in cyclone-wide mean moisture and rainfall rate with SST followed that expected from the Clausius-Clapeyron relation.

8 References

S. Bony, J.-L. Dufresne, H. Le Treut, J.-J. Morcrette and C. Senior. On dynamic and thermodynamic components of cloud changes. Climate Dynamics, 22, 71-86, doi 10.1007/s00382-003-0369-6

Bengtsson, L, Hodges, KI, Roeckner, E, 2006. Storm tracks and climate change journal of climate, 19 (15): 3518-3543.

Carnell R.E., and Senior C. A., 1998. Changes in mid-latitude variability due to increasing greenhouse gases and sulphate aerosols. Climate Dynamics, 14, 369-383.

Choi YS, Ho CH, Sui CH, 2005.Different optical properties of high cloud in GMS and MODIS observations. Geophysical Research Letters 32 (23): Art. No. L23823.

Collins, WD, Rasch, PJ, Boville, BA, Hack, JJ, McCaa, JR, Williamson, DL, Briegleb, BP, Bitz, CM, Lin, SJ, Zhang, MH. 2006. The formulation and atmospheric simulation of the Community Atmosphere Model version 3 (CAM3). J. Climate 19 (11): 2144-2161.

DelGenio, A. D., M. S. Yao, W. Kovari, and K. K. W. Lo, 1996: A prognostic cloud water parameterization for global climate models. J. Climate, 9, 270-304.

Field, PR, Wood, R. 2007a. Precipitation and cloud structure in midlatitude cyclones. J. Climate 20 (2): 233-254.

Field, PR, Wood, R. 2007b. Correction to 'Precipitation and cloud structure in midlatitude cyclones'. J. Climate in press.

Fu Q, Johanson CM, Wallace JM et al., 2006. Enhanced mid-latitude tropospheric warming in satellite measurements Science 312 (5777): 1179-1179.

Fyfe, J.C., 2003. Extratropical southern hemisphere cyclones: Harbingers of climate change? Journal of Climate, 16 (17): 2802-2805.

Harrold, T. W., 1990: Mechanisms influencing the distribution of precipitation within baroclinic disturbances. *Quart. J. Roy. Meteorol. Soc.*, **99**, 232-251.

Geng, QZ, Sugi, M, 2003. Possible change of extratropical cyclone activity due to enhanced greenhouse gases and sulfate aerosols - Study with a high-resolution AGCM Journal of Climate, 16 (13): 2262-2274.

Gettelman, A, Kinnison, D.E. 2007. The global impact of supersaturation in a coupled chemistry-climate model. Atmospheric Chemistry and Physics 7 (6): 1629-1643.

Gettelman, A., H. Morrison, and S. J. Ghan, 2007: A new two-moment bulk stratiform cloud microphysics scheme in the NCAR Community Atmosphere Model (CAM3), Part I: Single-column and global results. J. Climate. (submitted)

Hack, JJ, Caron, JM, Yeager, SG, Oleson, KW, Holland, MM, Truesdale, JE, Rasch, PJ. 2006. Simulation of the global hydrological cycle in the CCSM Community Atmosphere Model version 3 (CAM3): Mean features. Journal of Climate 19 (11): 2199-2221.

Hack, J.J, Boville, B.A., Kiehl, J.T., Rasch, P.J., Williamson, D.L. 1994. Climate statistics from the national center for atmospheric research community climate model CCM2. Journal of Geophysical Research-Atmospheres 99 (D10): 20785-20813.

Klein, SA, Jakob, C. 1999. Validation and sensitivities of frontal clouds simulated by the ECMWF model. Monthly Weather Review 127 (10): 2514-2531.

Lin, WY, Zhang, MH. 2004. Evaluation of clouds and their radiative effects simulated by the NCAR Community Atmospheric Model against satellite observations. Journal of Climate 17 (17): 3302-3318.

Morrison, H., and A. Gettelman, 2007: A new two-moment bulk stratiform cloud microphysics scheme in the NCAR Community Atmosphere Model (CAM3), Part I: Description and numerical tests. J. Climate. (submitted)

Norris, JR, Weaver, CP. 2001. Improved techniques for evaluating GCM cloudiness applied to the NCAR CCM3. Journal of Climate 14 (12): 2540-2550.

Oreopoulos L., 2005. The impact of subsampling on MODIS Level-3 statistics of cloud optical

thickness and effective radius IEEE Transactions on Geoscience and Remote Sensing 43 (2): 366-373.

Paciorek, CJ, Risbey, JS, Ventura, V, et al. 2002. Multiple indices of Northern Hemisphere cyclone activity, winters 1949-99 Journal of Climate, 15 (13): 1573-1590.

Randel, D. L., T. H. V. Haar, M. A. Ringerud, G. Stephens, T. J. Greenwald, and C. L. Combs, 1996: A new global water vapor dataset. Bull. Amer. Meteor. Soc., 77, 12331246.

Rasch P. J., and J. E. Kristjansson, 1998: A comparison of CCM3 model climate using diagnosed and predicted condensate parameterizations. J. Climate, 11, 1587-1614.

Sinclair, MR, Watterson, IG, 1999. Objective assessment of extratropical weather systems in simulated climates Journal of Climate, 12 (12): 3467-3485.

Slingo, J.M. 1987. the development and verification of a cloud prediction scheme for the ecmwf model. Quarterly Journal of the Royal Meteorological Society 113 (477): 899-927.

Wang, XLL, Swail, VR, Zwiers, FW, 2006. Climatology and changes of extratropical cyclone activity: Comparison of ERA-40 with NCEP-NCAR reanalysis for 1958-2001 Journal of Climate, 19 (13): 3145-3166.

Webb, M, Senior, C, Bony, S, Morcrette, JJ. 2001. Combining ERBE and ISCCP data to assess clouds in the Hadley Center, ECMWF and LMD atmospheric climate models. Climate Dynamics

17 (12): 905-922.

Weare, B.C. 1993. Multiyear statistics of selected variables from the isccp c2 data set. Quarterly Journal of the Royal Meteorological Society 119 (512): 795-808, part A.

Weaver, C.P., Ramanathan, V. 1995. Deductions from a simple climate model - factors governing surface-temperature and atmospheric thermal structure. Journal of Geophysical Research-Atmospheres 100 (D6): 11585-11591.

Xie, P., and P. A. Arkin, 1997: Global precipitation: A 17-year monthly analysis based on gauge observations, satellite estimates, and numerical model outputs. Bull. Amer. Meteor. Soc., 78, 25392558.

Yeager, SG, Shields, CA, Large, WG, Hack, JJ. 2006. The low-resolution CCSM3. Journal of Climate 19 (11): 2545-2566.

Yin JH, 2005. A consistent poleward shift of the storm tracks in simulations of 21st century climate. Geophysical Research Letters 32 (18): Art. No. L18701.

Zhang, G.J., McFarlane, N.A. 1995. Sensitivity of climate simulations to the parameterization of cumulus convection in the canadian climate center general-circulation model. Atmosphere-Ocean 33 (3): 407-446.

Zhang, MH, Lin, WY, Bretherton, CS, Hack, JJ, Rasch, PJ. 2003. A modified formulation of fractional stratiform condensation rate in the NCAR Community Atmospheric Model (CAM2). Journal of Geophysical Research-Atmospheres 108 (D1): doi:.

Figure 1: Composited satellite observations of rainfall rate derived from microwave data (AMSR-E) for midlatitude cyclones centered within a 4000km x 4000km domain. The composites are taken from the most moist and greatest strength categories. Composite mean sea level pressure (mb) and 10 m wind vectors obtained from Quikscat are also shown. Inset figure: Mean cyclone composite values within a 2000 km circle located at the domain center. The errorbars represent twice the estimate standard error for the mean value. Cyclone mean rain rate is plotted against rain rate derived from combining cyclone strength and atmospheric moisture with a moist warm conveyor belt argument (cyclone mean rain rate = $0.023\langle V\rangle\,\langle WVP\rangle$. The circles represent the results from seasonal composites: w: winter [boreal Dec-Feb (DJF), austral Jun-Aug (JJA), sp: spring [boreal Mar-May (MAM), austral Sep-Nov (SON)], su:summer [boreal JJA, austral DJF], f: fall [boreal SON, austral MAM], for all strength and moisture categories.

Figure 2: High-top (cloud top pressure <440 mb) composite cloud fraction in each 100km x100km grid cell for the satellite observations and different model configurations. The 4000km x 4000km domain composite is for the medium moisture, greatest strength category. The composite sea level pressure is overplotted (mb, solid lines))

Figure 3: High-top (cloud top pressure <440 mb) composite cloud fraction in each 100km x100km grid cell for the satellite observations and different model configurations. The cloud fraction is broken down into three optical thickness categories: thin (cirrus $\tau < 5$), intermediate (cirrostratus$5 < \tau < 25$), and thick (deep frontal $\tau > 25$).Mid-top (710 mb > cloud top pressure >440 mb) composite cloud fraction in each 100km x100km grid cell for the satellite observations and different model configurations. The cloud fraction is broken down into three optical thick-

ness categories: thin (altocumulus), intermediate (altostratus), and thick (nimbostratus).Low-top (710 mb $<$ cloud top pressure) composite cloud fraction in each 100km x100km grid cell for the satellite observations and different model configurations. The cloud fraction is broken down into three optical thickness categories: thin (cumulus), intermediate (stratocumulus), and thick (stratus). The 4000km x 4000km domain composites are generated from all of the cyclones found in the North Pacific region.

Figure 4: Mean composite high-top cloud fraction as a function of cyclone strength in the 9 strength and moisture categories for the satellite observations and model configurations. The typical 2x standard error in the mean is also indicated.

Figure 5: Composite rainfall rate in each 100km x100km grid cell for the satellite observations and different model configurations. The 4000km x 4000km domain composite is for the medium moisture, greatest strength category. The composite sea level pressure is overplotted (mb, solid lines))

Figure 6: For the satellite observations and model configurations, mean composite values of various parameters are plotted. a) Rainfall rate versus cyclone strength. b) Rainfall rate versus predicted warm conveyor rainfall rate. c) Column integrated water vapor path versus sea surface temperature. The typical 2x standard errors in the mean are also indicated in each panel.

Figure 7: a) For each strength category the ratio of the measured mean composite moisture to the medium measured moisture is plotted against the difference in measured SST from the SST

in the medium moisture category. Standard errors for the mean values are given (gray bars). The dashed line represents a change in $< WVP >$ of 6.5% per K. The dot-dash line represents a change in $< WVP >$ of 9% per K: the expected change in $< WVP >$ from the Clausius-Clapeyron (C-C) relation when both temperature and the moist adiabatic lapse rate vary. Results are shown for the satellite observations and different model configurations. b) Same as (a), but for rainfall rate.

Figure 8: Composite cloud liquid water path in each 100km x100km grid cell for the satellite observations and different model configurations. The 4000km x 4000km domain composite is for the medium moisture, greatest strength category. The composite sea level pressure is overplotted (mb, solid lines))

Figure 9: Top left panel:Scatter plot of cyclone strength (mean windspeed within 2000km of cyclone center $\langle V \rangle$) and atmospheric moisture (mean water vapor path within 2000km of cyclone center $\langle WVP \rangle$). The circles represent all of the cyclones located within the four regions ($\sim$ 1500). The grey circles represent the subset of circles used in the conditional sampling that satisfy the following relation $((log_{10}(\langle V \rangle) - \overline{log_{10}(\langle V \rangle)})/0.2)^2 + ((log_{10}(\langle WVP \rangle) - \overline{log_{10}(\langle WVP \rangle)})/0.25)^2 < 1$, where $\overline{log_{10}(\langle V \rangle)}$(=0.89) and $\overline{log_{10}(\langle WVP \rangle)}$(=1.27) are mean values from the whole database. The dotted lines delineate the boundaries of the nine bins used in the conditional sampling. The use of a subset of the cyclones ensures that there is no monotonic variation in the mean variables along each row and column. The remaining panels show the relative frequency of cyclones within the 9 strength and moisture categories for the satellite and different model configurations. The total number of cyclones is given in the title of each panel. The gray

scale relates to the relative frequency: light – low, dark – high.

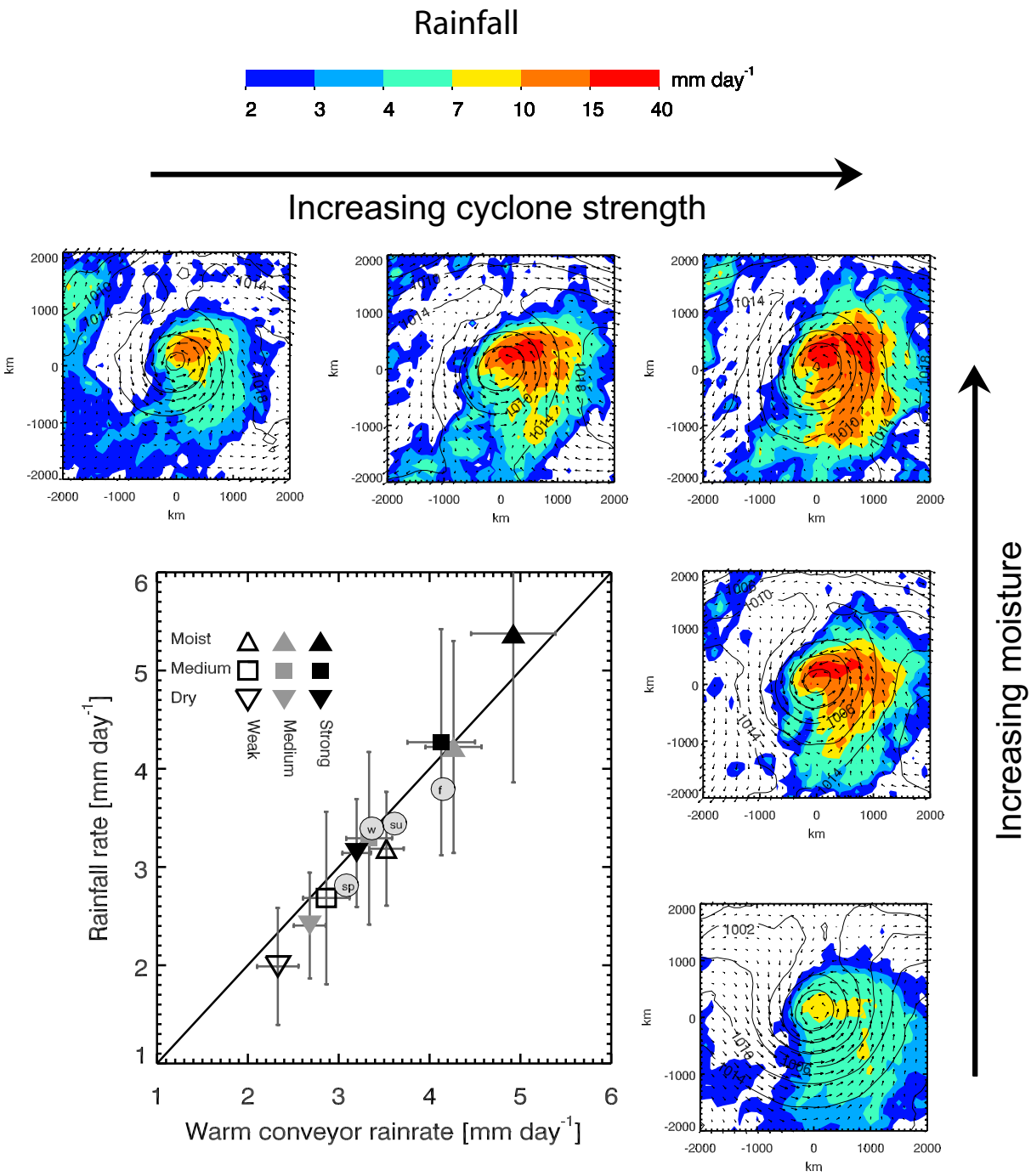

Figure 1: Composited satellite observations of rainfall rate derived from microwave data (AMSR-E) for midlatitude cyclones centered within a 4000km x 4000km domain. The composites are taken from the most moist and greatest strength categories. Composite mean sea level pressure (mb) and 10 m wind vectors obtained from Quikscat are also shown. Inset figure: Mean cyclone composite values within a 2000 km circle located at the domain center. The errorbars represent twice the estimate standard error for the mean value. Cyclone mean rain rate is plotted against rain rate derived from combining cyclone strength and atmospheric moisture with a moist warm conveyor belt argument (cyclone mean rain rate = $0.023\langle V\rangle\,\langle WVP\rangle$. The circles represent the results from seasonal composites: w: winter [boreal Dec-Feb (DJF), austral Jun-Aug (JJA), sp: spring [boreal Mar-May (MAM), austral Sep-Nov (SON)], su:summer [boreal JJA, austral DJF], f: fall [boreal SON, austral MAM], for all strength and moisture categories.

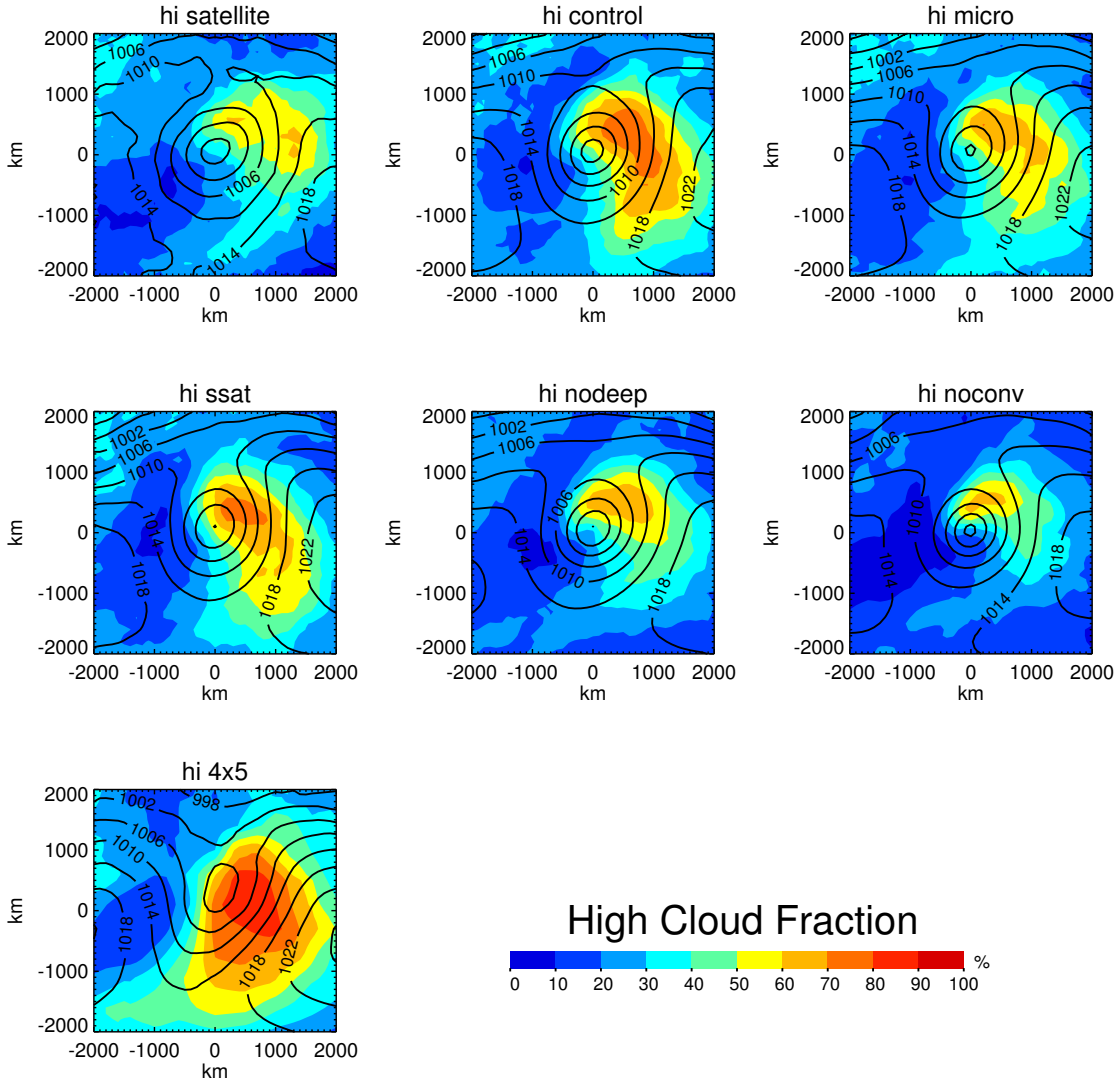

Figure 2: High-top (cloud top pressure <440 mb) composite cloud fraction in each 100km x100km grid cell for the satellite observations and different model configurations. The 4000km x 4000km domain composite is for the medium moisture, greatest strength category. The composite sea level pressure is overplotted (mb, solid lines))

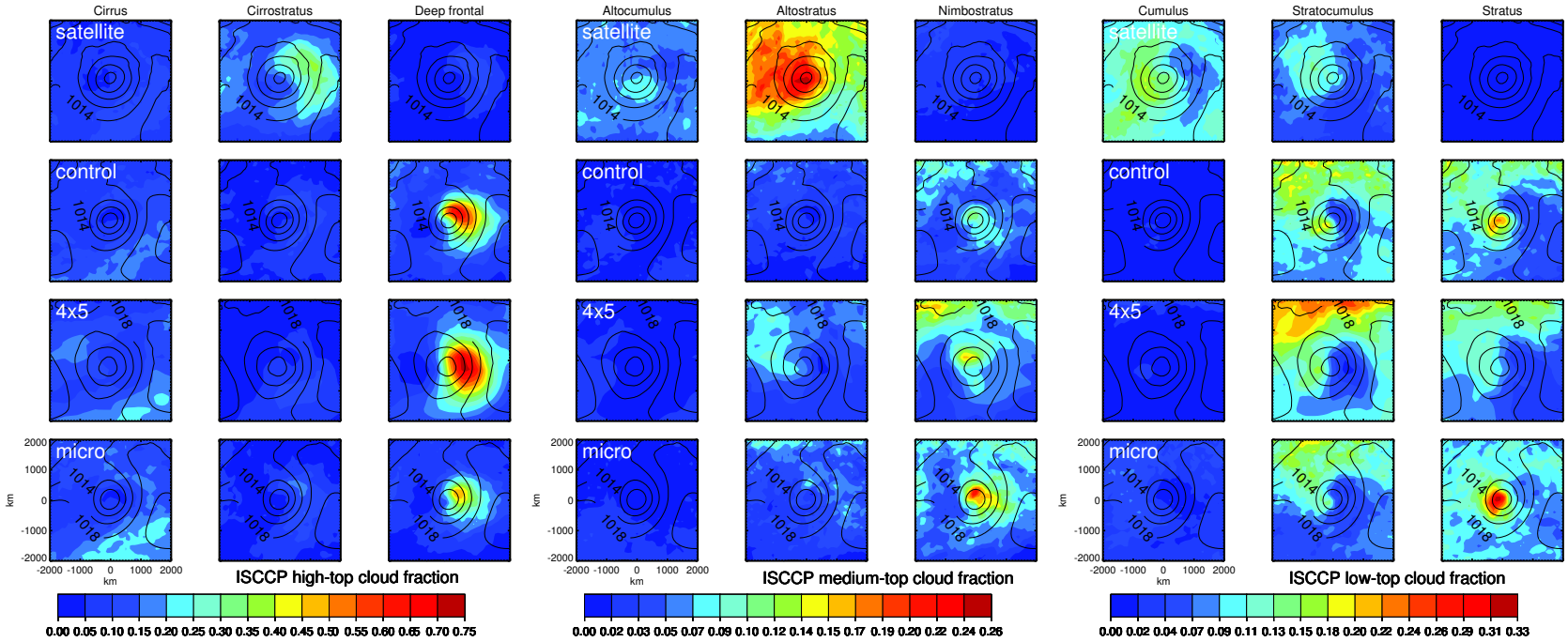

Figure 3: High-top (cloud top pressure <440 mb) composite cloud fraction in each 100km x100km grid cell for the satellite observations and different model configurations. The cloud fraction is broken down into three optical thickness categories: thin (cirrus $\tau < 5$), intermediate (cirrostratus$5 < \tau < 25$), and thick (deep frontal $\tau > 25$).Mid-top (710 mb > cloud top pressure >440 mb) composite cloud fraction in each 100km x100km grid cell for the satellite observations and different model configurations. The cloud fraction is broken down into three optical thickness categories: thin (altocumulus), intermediate (altostratus), and thick (nimbostratus).Low-top (710 mb < cloud top pressure) composite cloud fraction in each 100km x100km grid cell for the satellite observations and different model configurations. The cloud fraction is broken down into three optical thickness categories: thin (cumulus), intermediate (stratocumulus), and thick (stratus). The 4000km x 4000km domain composites are generated from all of the cyclones found in the North Pacific region.

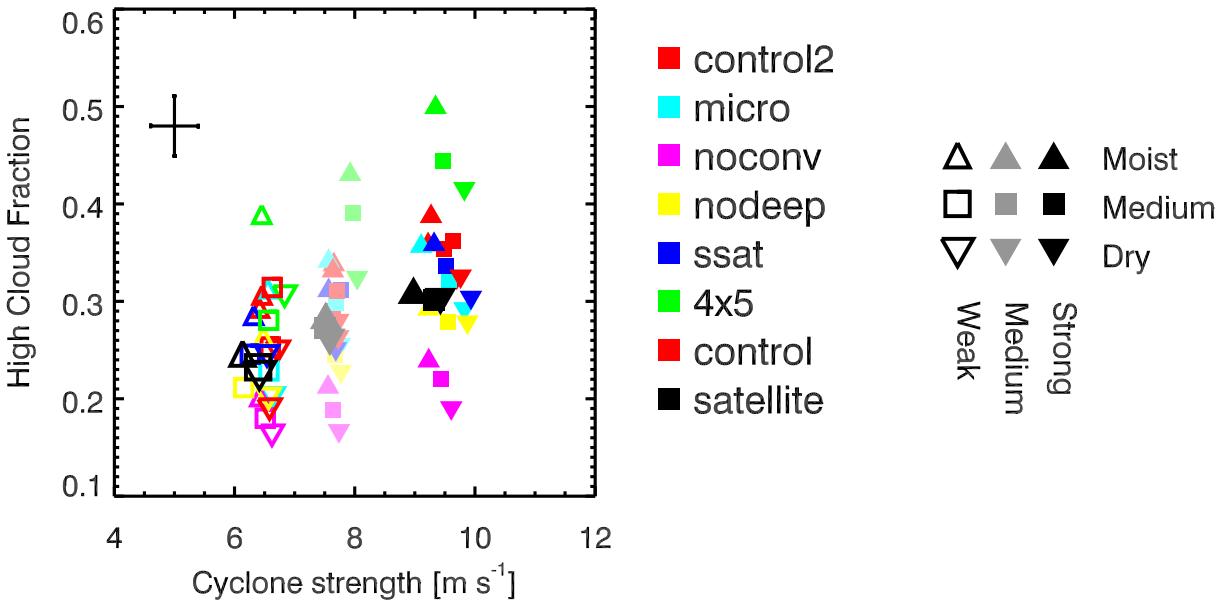

Figure 4: Mean composite high-top cloud fraction as a function of cyclone strength in the 9 strength and moisture categories for the satellite observations and model configurations. The typical 2x standard error in the mean is also indicated.

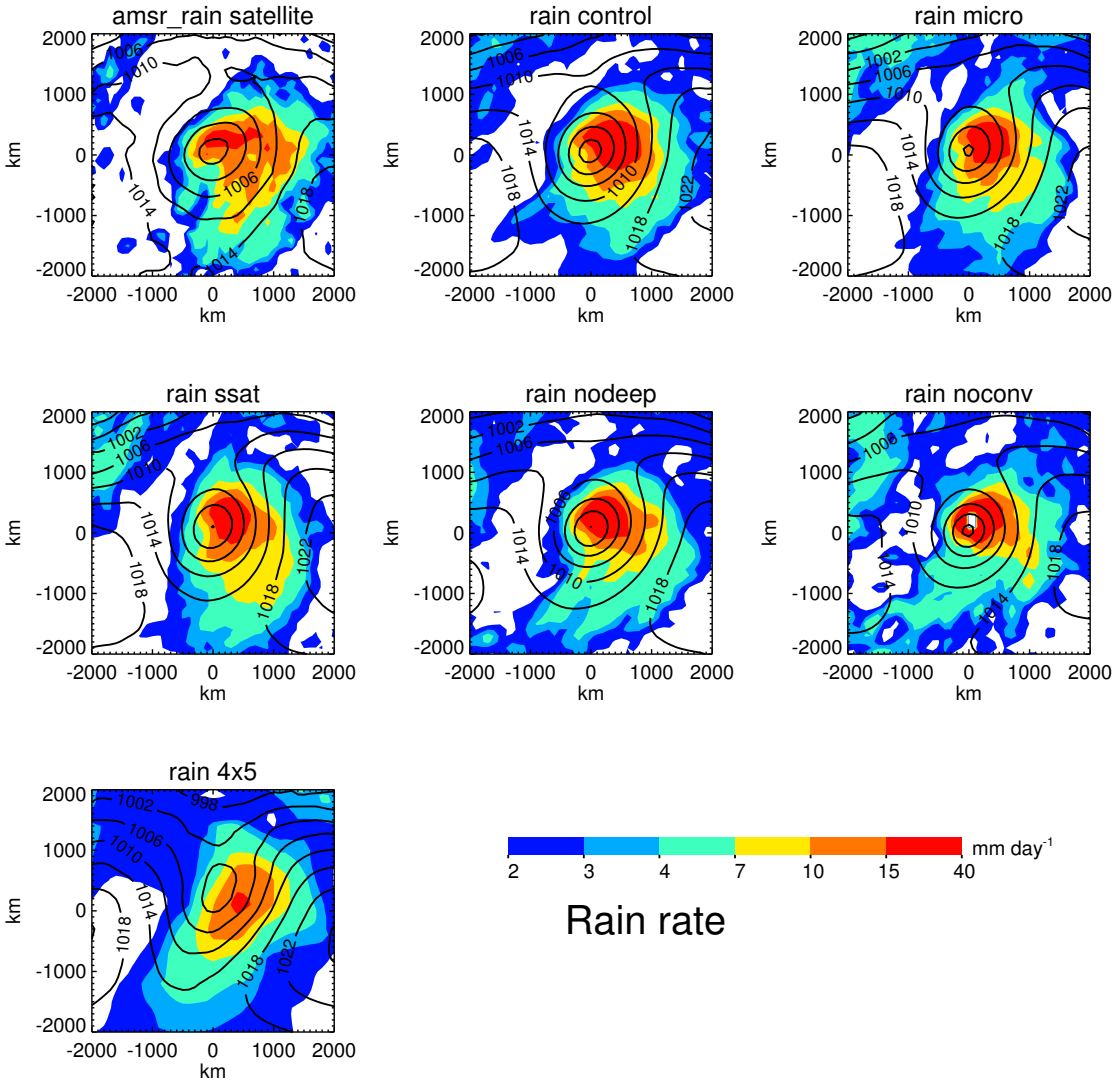

Figure 5: Composite rainfall rate in each 100km x100km grid cell for the satellite observations and different model configurations. The 4000km x 4000km domain composite is for the medium moisture, greatest strength category. The composite sea level pressure is overplotted (mb, solid lines))

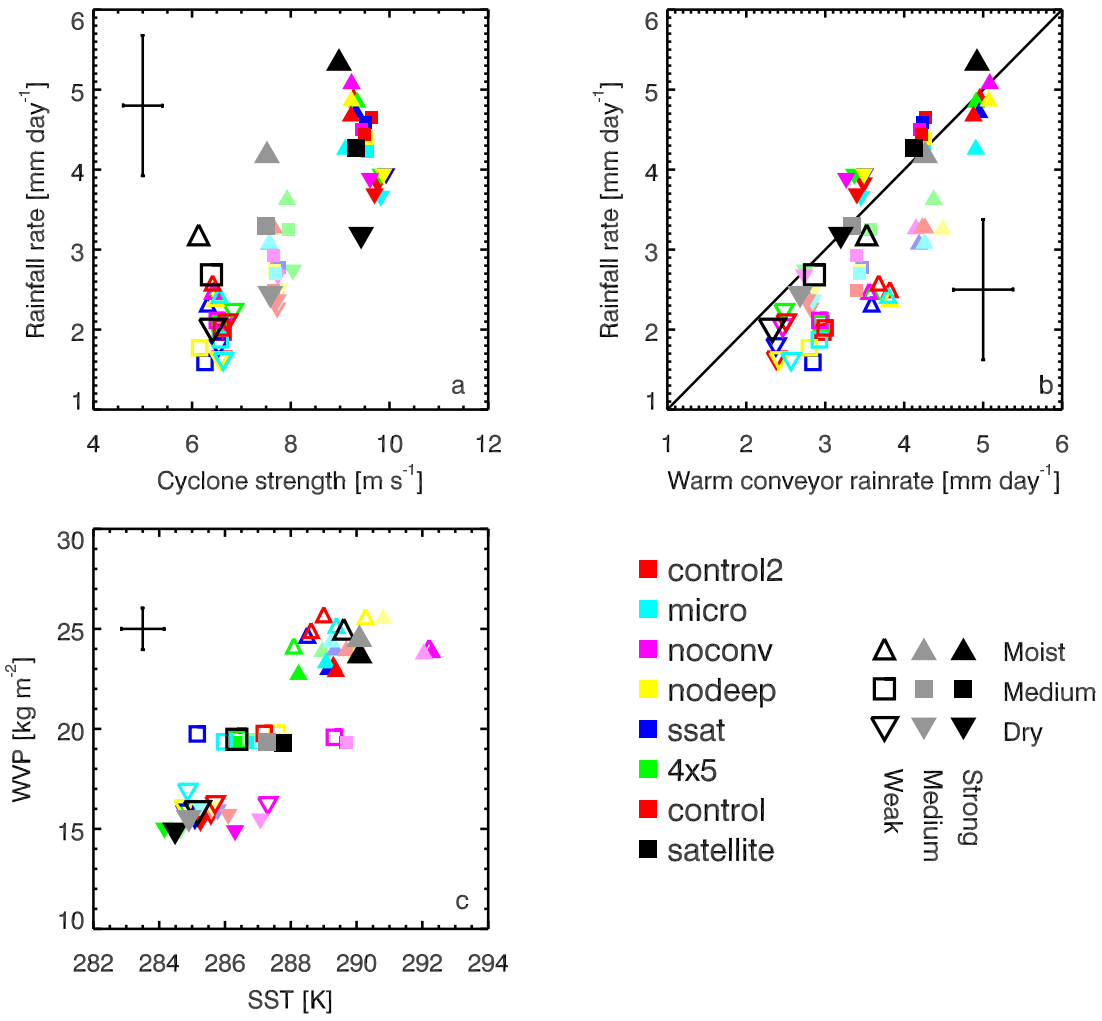

Figure 6: For the satellite observations and model configurations, mean composite values of various parameters are plotted. a) Rainfall rate versus cyclone strength. b) Rainfall rate versus predicted warm conveyor rainfall rate. c) Column integrated water vapor path versus sea surface temperature. The typical 2x standard errors in the mean are also indicated in each panel.

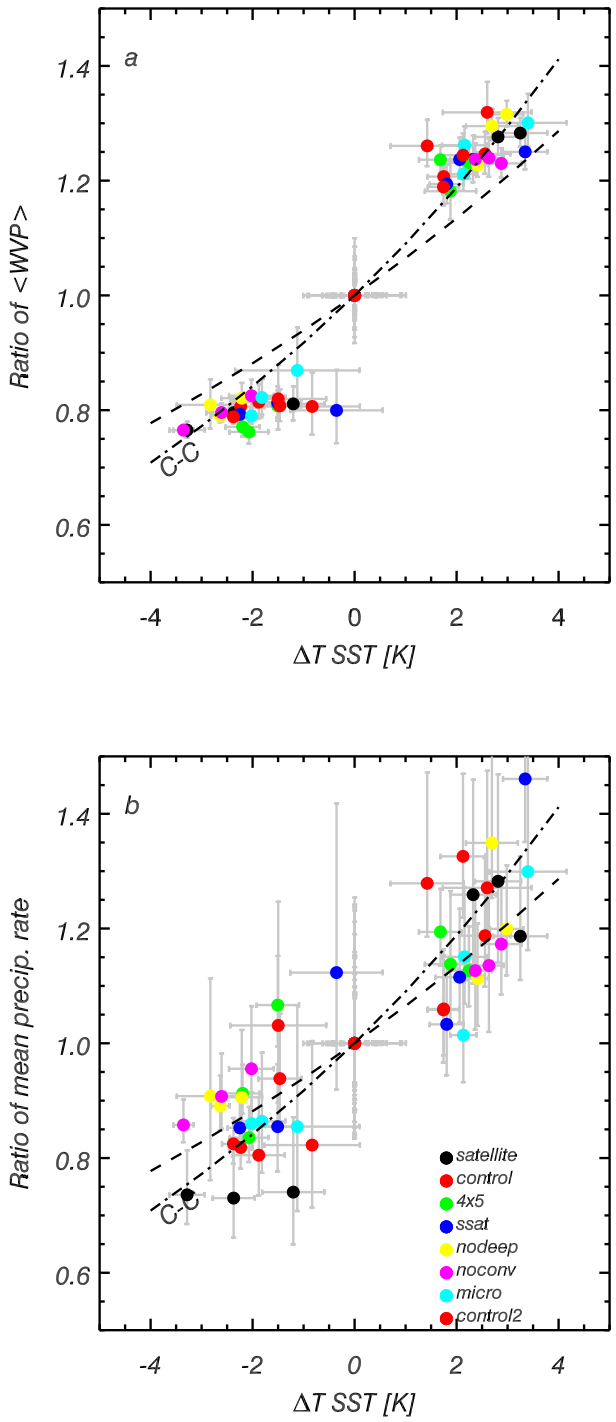

Figure 7: a) For each strength category the ratio of the measured mean composite moisture to the medium measured moisture is plotted against the difference in measured SST from the SST in the medium moisture category. Standard errors for the mean values are given (gray bars). The dashed line represents a change in $< WVP >$ of 6.5% per K. The dot-dash line represents a change in $< WVP >$ of 9% per K: the expected change in $< WVP >$ from the Clausius-Clapeyron (C-C) relation when both temperature and the moist adiabatic lapse rate vary. Results are shown for the satellite observations and different model configurations. b) Same as (a), but for rainfall rate.

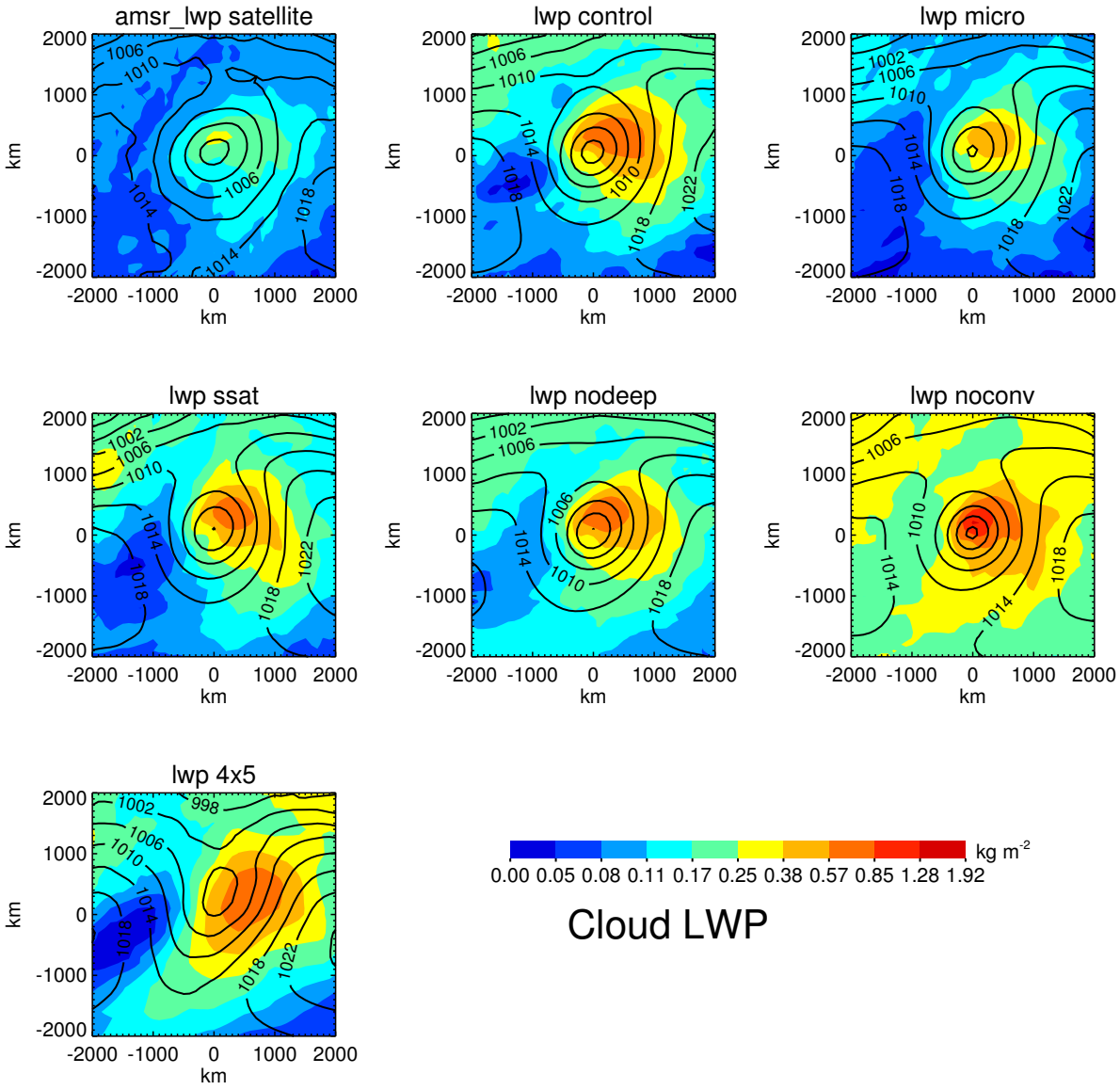

Figure 8: Composite cloud liquid water path in each 100km x100km grid cell for the satellite observations and different model configurations. The 4000km x 4000km domain composite is for the medium moisture, greatest strength category. The composite sea level pressure is overplotted (mb, solid lines))

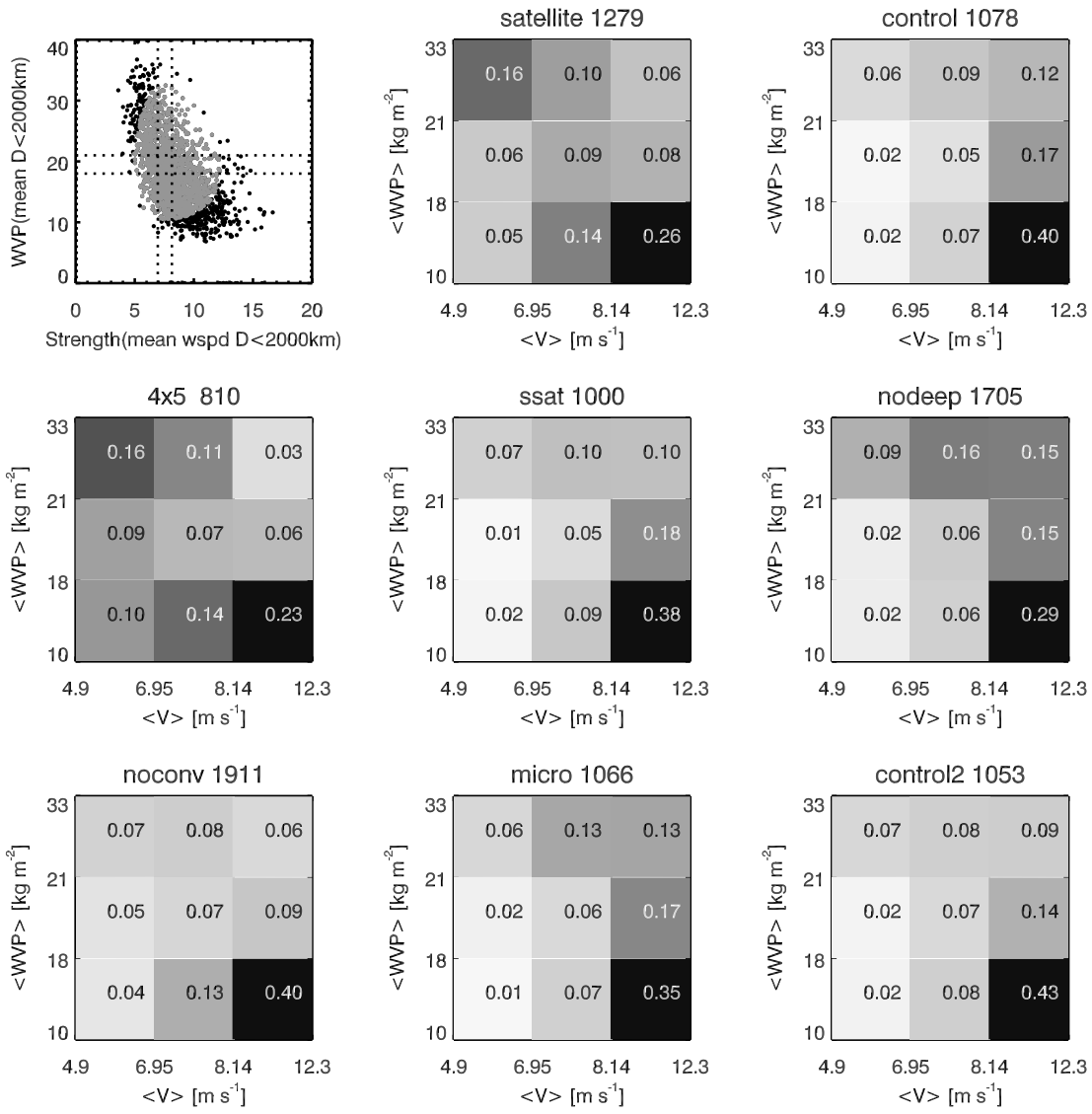

Figure 9: Top left panel:Scatter plot of cyclone strength (mean windspeed within 2000km of cyclone center $\langle V \rangle$) and atmospheric moisture (mean water vapor path within 2000km of cyclone center $\langle WVP \rangle$). The circles represent all of the cyclones located within the four regions ($\sim$ 1500). The grey circles represent the subset of circles used in the conditional sampling that satisfy the following relation $((log_{10}(\langle V \rangle) - \overline{log_{10}(\langle V \rangle)})/0.2)^2 + ((log_{10}(\langle WVP \rangle) - \overline{log_{10}(\langle WVP \rangle)})/0.25)^2 < 1$, where $\overline{log_{10}(\langle V \rangle)}$(=0.89) and $\overline{log_{10}(\langle WVP \rangle)}$(=1.27) are mean values from the whole database. The dotted lines delineate the boundaries of the nine bins used in the conditional sampling. The use of a subset of the cyclones ensures that there is no monotonic variation in the mean variables along each row and column. The remaining panels show the relative frequency of cyclones within the 9 strength and moisture categories for the satellite and different model configurations. The total number of cyclones is given in the title of each panel. The gray scale relates to the relative frequency: light – low, dark – high.